Ice accretion and aerodynamic effects on a multi-element airfoil under SLD icing conditions

L. Prince Raj*, J. W. Lee* and R. S. Myong*,†

*School of Aerospace and Software Engineering, Gyeongsang National University, Jinju, Gyeongnam, 52828, South Korea

† Research Center for Aircraft Core Technology and ReCAPT, Gyeongsang National University, Jinju, Gyeongnam 52828, South Korea

myong@gnu.ac.kr

Summary: The impingement behavior of large water droplets, their interactions with the solid wall and the subsequent ice accretion and aerodynamic effects have become a key issue in in-flight aircraft icing. In this study, ice accretion and aerodynamic effects on a multi-element airfoil were investigated under the recently introduced Appendix O icing envelope. Supercooled large droplet (SLD) dynamics were taken into account by employing a unified computational approach. Ice accretion was simulated using a partial differential equation (PDE) based solver, instead of the commonly used control volume method. The numerical solver of the SLD impingement was built on the droplet deformation and droplet-wall interaction splash models. The unified solvers for clean air, large droplet impingement, ice accretion, and the aerodynamic analysis of ice effects—all of which are based on a single unstructured upwind finite volume framework—were first validated using available experimental data and then applied to investigate ice accretion and the resulting aerodynamic effects on multi-element airfoils for various flight conditions and, in particular, near-freezing SLD icing conditions. Interestingly, two counter-intuitive results were found when comparing the ice accretion and associated aerodynamic degradation for non-SLD and SLD cases. Moreover, considering runback ice was shown to be essential in the design of an ice protection system (IPS) for the multi-element wing.

Key Words: Aircraft icing, supercooled large droplet (SLD), multi-element airfoil

Nomenclature

c = length of the chord (m)

C_D = drag coefficient of droplet

$Cp,_{ice}$ = specific heat at constant pressure for ice (J/kg/K)

$Cp,_w$ = specific heat at constant pressure for water (J/kg/K)

e = eccentricity, $e = 1 - \left(1 + 0.07We_b^{0.5}\right)^{-6}$

f_m = mass ratio of ejected and initial droplet

f_u = velocity ratio of ejected and initial droplet

$f_{u,t}$ = tangential droplet velocity ratio

$f_{u,n}$ = normal droplet velocity ratio

$\boldsymbol{g}$ = gravity vector

h_C = convective heat transfer coefficient (W/m^{2}K)

h_f = film thickness (m)

La = Laplace number, $La = Re^2/We$.

L_{evap} = latent heat of evaporation (J/kg)

L_{fusion} = latent heat of fusion (J/kg)

L_{subl} = latent heat of sublimation (J/kg)

LWC = liquid water content (g/m^3)

M = Mach number

m_s = droplet ejected mass (Kg)

m_0 = droplet initial mass (Kg)

$\dot{m}_{evap}$ = instantaneous mass of evaporation (kg/s)

$\dot{m}_{ice}$ = instantaneous mass of ice accretion (kg/s)

MVD = mean volumetric diameter (m)

$\boldsymbol{n}$ = unit vector normal to the surface

Oh = Ohnesorge number, $Oh = \mu_w \Big/ \sqrt{MVD\rho_w\sigma}$

Re = droplet Reynolds number

T_C = freezing point (T_C = 273.15 K)

T_{equi} = temperature at wall/water/ice/air interface (K)

$\tilde{T}_{d,\infty}$ = free stream droplet temperature (℃)

T_∞ = free stream air temperature (K)

t = time (s)

U_∞ = free stream air velocity (m/s)

$\boldsymbol{u}$ = droplet velocity vector

$\boldsymbol{u}_g$ = air velocity vector

$\boldsymbol{u}_d$ = droplet impact velocity (m/s)

$\bar{\boldsymbol{u}}_f$ = mean velocity of the water film (m/s)

$\boldsymbol{u}_0$ = pre-impact velocity of droplet

$\boldsymbol{u}_s$ = post-impact velocity of droplet

$u_{t,s}$ = tangential component of post impact velocity (m/s)

$u_{n,s}$ = normal component of post impact velocity (m/s)

$u_{t,o}$ = tangential component of pre-impact velocity (m/s)

$u_{n,s}$ = normal component of pre-impact velocity (m/s)

We = breakup Weber number, $We_b = \rho_g.MVD.\left|\boldsymbol{u}_a - \boldsymbol{u}_d\right|^2 \big/ \sigma$

We_S = impact Weber number , $We_S = \rho_g.MVD.\boldsymbol{u}_d^{\,2} \big/ \sigma$

β = collection efficiency

ε = solid emissivity

μ = dynamic viscosity of air (Ns/m^2)

μ_w = dynamic viscosity of water (Ns/m^2)

ρ = density of droplets in terms of LWC (Kg/m^3)

ρ_a = air density (kg/m^3)

ρ_w = water density (kg/m^3)

ρ_{in} = density of droplets at a cell adjacent to the wall (kg/m^3)

σ = surface tension (N/m)

σ_a = Boltzmann constant (σ_a = 1.38064852 × 10^{-23} m^2 kg s^{-2} K^{-1})

τ_{wall} = air wall shear stress (N/m^2)

θ_0 = angle of incidence of the droplet in radians

1. Introduction

In Earth's atmosphere, diluted water droplets can be observed in the airflow around aircraft flying inside clouds [1, 2]. Exposure to these supercooled water droplets for a considerable period may cause significant ice accretion on the surfaces of critical components including wings, rotor blades, engine inlet, air data systems (ADS), windshield, and propeller [3], as illustrated in Fig. 1 (left). This accumulated ice can result in degraded aerodynamic and propulsive performances and serious safety concerns [4]. Understanding large droplet impact behavior, described in Fig. 1 (right), and determining ice accretion on solid surfaces can be essential to designing proper ice protection systems (IPS) to prevent (anti-) and remove (de-) ices formed on the surfaces of aircraft.

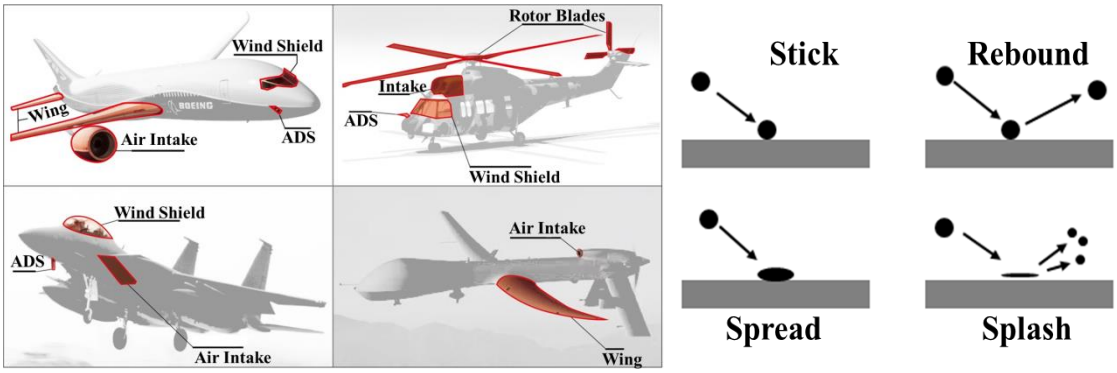

Figure 1 Ice accumulation prone area (left) and surface interaction of large droplets (right) on aircraft

Data on ice accretion can be obtained by using an icing wind tunnel test [5] or state-of-the-art CFD simulation [6, 7]. Because it offers the versatility to analyze any scenario/condition as well as low cost and is free from scaling issues, the CFD-based aerodynamic, icing, and thermal simulation has increasingly become mainstream methods for obtaining information on droplet impingement and ice accretion.

As illustrated in Fig. 2, several critical parameters affect ice accretion, and these parameters exert a strong influence on the accumulation of ice. In the aviation community, icing conditions are specified based on the distribution of droplet sizes, known as mean volume diameter (MVD), which is in the range of 40 micrometers or less. However, in some atmospheric conditions, the

droplet size may reach 40 micrometers to 400 micrometers, and this is known as a supercooled large droplet (SLD). Since the ATR-72 commuter aircraft accident [8] in 1994, interest in the study of SLD icing has grown significantly due to its complex physics and large impact on the safety of aircraft. After lengthy consideration, the FAA finally introduced the new Appendix O regulations in November 2014 in order to accommodate SLD icing conditions.

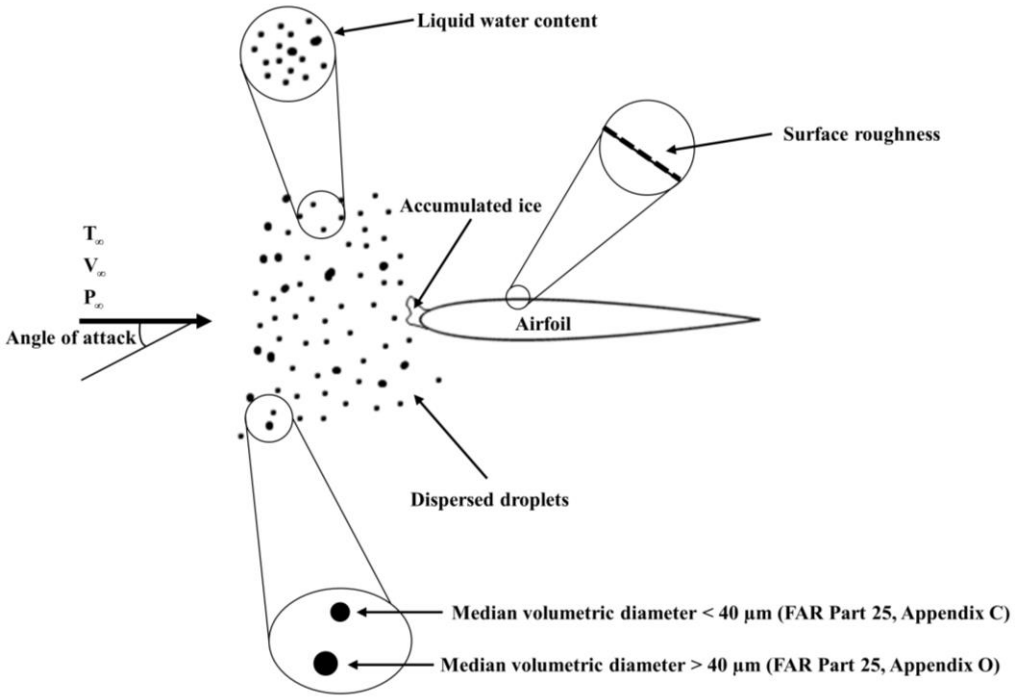

Figure 2 Parameters affecting ice accretion and icing certification appendices for different droplet diameters

The effects of SLD icing specified in Appendix O can be more severe and unpredictable than conventional icing by smaller droplets and can occur at different locations on the aircraft. Since more ice growth is possible under SLD icing conditions, the conventional IPS designed under non-SLD icing conditions defined in Appendix C may not provide enough energy to fully clear the ice and liquid water, which may lead to dangerous runback ice accretions. Hence, the SLD icing effects must be taken into account during the design of IPS, for example, by determining the protection area and power requirements. Moreover, according to the current icing regulation, the analysis and design of ice protection system should demonstrate that no hazardous quantity of ice will form on surfaces that are critical to the safe operation of the aircraft when exposed to the icing conditions in Appendices C and O [9, 10].

Modern transport aircraft are usually equipped with a multi-element wing in order to meet the need for high lift at low speeds and high angles of attack [11]. The slat located ahead of the main element delays flow separation which enables the wing to operate at higher angles of attack without significant performance penalties. Most commercial aircraft, due to maintenance and manufacturing complexity, employ three elements, rather than four or more elements.

The multi-element wing is activated during take-off and landing, to enhance lift in the former and to lower the stall speed in the latter. Ice accretion on the multi-element wing during take-off and landing can affect the climbing and landing performance significantly. In the past, it was known from an experimental study by Valarezo [12] that the percentage losses for multi-element airfoils in general are not as severe as for single-element configurations. Several other studies have also been conducted to investigate SLD effects [13]. However, there are a limited set of investigations on multi-element airfoils, in particular, under SLD icing conditions [7, 14, 15]. *There are very few studies to investigate aerodynamic performance degradation of multi-element airfoil, in particular, under critical near-freezing SLD icing conditions.*

In this study, ice accretion and aerodynamic effects on a multi-element airfoil under the recently introduced SLD icing conditions were investigated in detail. For this purpose, new unified solvers of clean air, large droplet impingement, ice accretion, and the aerodynamic analysis of ice effects—all of which are based on a single unstructured positivity-preserving upwind finite volume framework—were developed. Computational simulations of the multi-element airfoil under SLD and non-SLD conditions were then conducted to verify the capability of the new method. Finally, ice accretion and consequential aerodynamic effects on the multi-element airfoil were investigated for various flight and icing conditions, in particular, near-freezing SLD conditions.

2. Physical and Computational Models

Computational models of atmospheric droplets fall into two categories, the clean airfield, and air-mixed droplet field. For this kind of flow, in general, the two-phase flow can further be simplified by ignoring the droplet effects on air flows. Since the mass loading ratio of the bulk

density of the droplets over the bulk density of air is on the order of 10^{-3} in the air-droplet flow, the two-phase flow can be simulated using a weakly coupled (one-way coupling) algorithm [16]. The air flow data should then be provided to the droplet solver through the source terms in the case of the Eulerian droplet equations.

As the clean air solver, the compressible Navier-Stokes-Fourier (NSF) equations are employed along with the *k*-epsilon turbulence model including standard wall function. A Riemann invariant is implemented for the far-field boundary condition, while a no-slip boundary condition is imposed on solid surfaces. For solving NSF equations, the convective fluxes are calculated by Roe's approximate Riemann solver, and the Green-Gauss viscous treatment is applied for viscous flux. A shallow water droplet model developed in a previous work [6] based on the Eulerian framework was employed for the present second-order positivity-preserving droplet solver, together with the drag deformation and droplet wall interaction models. In the present weakly coupled algorithm, the Eulerian droplet solver is provided with the air flow information computed by the air flow solver through the source term. The shallow water droplet equations are derived as follows,

$$\begin{bmatrix} \rho \\ \rho \mathbf{u} \end{bmatrix}_t + \nabla \cdot \begin{bmatrix} \rho \mathbf{u} \\ \rho \mathbf{u}\mathbf{u} + \rho g d \mathbf{I} \end{bmatrix} = \begin{bmatrix} 0 \\ \mathbf{S}_D + \mathbf{S}_G + \mathbf{S}_S \end{bmatrix}. \tag{1}$$

Here, $\mathbf{S}_G=\rho g[0, 0, 1-\rho_g/\rho_w]^T$ is the resultant force of the gravity and buoyancy of droplets and the term $\mathbf{S}_D=A_u(\boldsymbol{u}_g - \boldsymbol{u})$ denotes the drag on droplets caused by the airflow. And, $\mathbf{S}_S = \nabla \cdot (\rho g d)\mathbf{I}$ is the added source term to circumvents the non-strictly hyperbolic nature of the droplet equations. The coefficient A_d can be expressed as,

$$A_d = 0.75 \cdot \rho \cdot C_D \cdot Re \cdot \mu / \rho_w \cdot MVD^2, \quad Re = \rho_g \cdot MVD \cdot \left| \boldsymbol{u}_g - \boldsymbol{u} \right| / \mu. \tag{2}$$

The drag coefficient can be obtained from Lapple [17] as follows,

$$C_D = \frac{24}{Re}\left(1 + 0.0197 Re^{0.63} + 2.6\mathrm{e}^{-4} \cdot Re^{1.38}\right), \tag{3}$$

which is valid for Re<1000. In order to solve the Eulerian based shallow water droplet equations, approximate Riemann solver HLLC is employed for flux calculation. A five-stage Runge-Kutta

temporal discretization is implemented.

The ice accretion solver was developed using the Messinger model [18], in particular, based on a partial differential equation (PDE) formulation, instead of the commonly used control volume method [19]. When implementing the high-fidelity PDE based thermodynamic model is based on the ICE3D module of FENSAP-ICE [20, 21], a recalibrated equation is used to avoid the different units in both sides of the original energy equations. The revised equation can be written as,

$$\frac{\partial \boldsymbol{U}}{\partial t} + \nabla \cdot \boldsymbol{F}\left(\boldsymbol{U}\right) = \boldsymbol{S}, \tag{4}$$

Eq. (4) can be written as

$$\boldsymbol{U} = \begin{bmatrix} h_f \\ h_f T_{equi} \end{bmatrix}, \ \boldsymbol{F}\left(\boldsymbol{U}\right) = \begin{bmatrix} \frac{h_f^2}{2\mu_w}\tau_{wall} \\ \frac{h_f^2 T_{equi}}{2\mu_w}\tau_{wall} \end{bmatrix}, \boldsymbol{S} = \begin{bmatrix} \frac{S_M}{\rho_w} \\ \frac{S_E}{\rho_w Cp_{,w}} + \frac{T_c S_M}{\rho_w} \end{bmatrix}. \tag{5}$$

$$\begin{aligned} S_M &= U_\infty LWC_\infty \beta - \dot{m}_{evap} - \dot{m}_{ice}, \\ S_E &= \left[Cp_{,w}\tilde{T}_{d,\infty} + \frac{\left\|\vec{u}_d\right\|^2}{2} \right] \times U_\infty LWC_\infty \beta - L_{evap}\dot{m}_{evap} \\ &\quad + \dot{m}_{ice}\left[L_{fus} - Cp_{,ice}T_{equi} \right] + h_c\left(T_{equi} - T_\infty\right) + \sigma_o \varepsilon \left[T_{equi}^4 - T_\infty{}^4 \right]. \end{aligned} \tag{6}$$

Through the assumption of a linear velocity distribution within the film, the velocity of the water film $\left(\bar{\mathbf{u}}_f\right)$ can be represented as a function of the water film thickness and shear stress as

$$\bar{\mathbf{u}}_f = f\left(h_f\right) = \frac{1}{h_f}\int_0^{h_f} u_f dh = \frac{h_f}{2\mu_w}\tau_{wall}. \tag{7}$$

The clean air solver provides the shear stress and heat flux as input to the ice accretion solver. The shallow water type droplet solver provides the droplet impact velocity and collection efficiency as input to the ice accretion solver. There are three unknowns to be computed: water film thickness (h_f), equilibrium temperature (T_{equi}), and mass accumulation ($\dot{m}_{ice}$). Since there are only two governing equations available, compatibility relations are necessary to close the system. Based on the physical behavior, the following compatibility equations can be derived as

$$h_f \geq 0, \dot{m}_{ice} \geq 0, h_f T_{equi} \geq h_f T_C, \dot{m}_{ice} T_{equi} \leq \dot{m}_{ice} T_C. \tag{8}$$

The first compatibility relation ensures that the film thickness remains positive. The second compatibility relation prevents the melting of accreted ice. The third compatibility relation enforces that the water film only can exist for equilibrium temperature above freezing point. Finally, the fourth compatibility equation stipulates that the ice cannot form for equilibrium temperatures above freezing point. By using these compatibility equations, each cell of the domain is explicitly solved individually with small time steps. The governing equations together with the compatibility relations for the water film on the surface of the body are solved by a cell center based a finite volume method. The computation elements are spread over the surface of the body and need to be solved using some numerical technique. The Roe's approximate Riemann solver is used to discretize the divergence terms in the governing equations.

Overall, all of the essential solvers for clean air, large droplet impingement, ice accretion, and aerodynamic analysis of ice effects were developed within a unified computational framework based on an unstructured finite volume method in which all the information can be easily communicated in a single grid system during the simulation.

3. Mathematical Model of Large Droplet in Appendix O

Under SLD conditions, additional effects associated with large droplet dynamics have to be taken into account in the computational modeling. In the present work, the droplet splashing, bouncing, and drop deformation depicted in Fig. 1 (right) are considered by introducing suitable semi-empirical formulations. Under the intense aerodynamic shear force and pressure gradients in the air-mixed droplet flow, large droplets may experience substantial configuration change, from spherical to non-spherical, and a subsequent change in aerodynamic drag. By interpolating the drag coefficients of the sphere ($C_{D_{Sphere}}$) and the oblate disk ($C_{D_{Disk}}$), depending on the value of eccentricity, the effective drag coefficient of the deformed droplet can be evaluated [22]:

$$C_D = (1-e) C_{D_{Sphere}} + e C_{D_{Disk}}. \tag{9}$$

The droplet behaves as a sphere at low Weber numbers (We_b), while it is closer to an oblate disk at higher Weber numbers. The drag coefficients of the sphere and the oblate disk can be

summarized for different Reynolds numbers.

A careful reassessment is necessary for modeling the solid wall boundary conditions to determine the droplet impingement. Once the projection of a normal vector on a solid surface and the droplet velocity in an adjacent cell on the solid surface are positive, the droplets should not collide with the solid surface. In contrast, if the projection is negative, the droplets should collide with the solid surface. When the size of the droplets is less than 40 micrometers, the following boundary conditions on a solid surface are defined as

$$\begin{aligned} &\rho_{wall} = \rho_{in},\ \boldsymbol{u}_{wall} = \boldsymbol{u}_0 \ \text{ if } \ \boldsymbol{u}\cdot\vec{n} \le 0, \\ &\rho_{wall} = 0,\ \boldsymbol{u}_{wall} = 0 \ \text{ if } \ \boldsymbol{u}\cdot\vec{n} \ge 0. \end{aligned} \tag{10}$$

The boundary conditions using Eq. (10) can be used to resolve a small droplet size. However, Eq. (10) cannot sufficiently simulate the SLD effects of the droplet-wall interactions. Hence for a large droplet simulation, wall boundary condition is modified to account the mass loss due to splashing and secondary droplet velocity vectors. Therefore, modification of the boundary condition considering the SLD effects is used if the projection of the normal vector and the velocity vector is negative. It can be expressed as,

$$\rho_{wall} = (1 - f_m)\rho_{in},\ \boldsymbol{u}_{wall} = \boldsymbol{u}_S, \quad \text{if } \ \boldsymbol{u}\cdot\mathbf{n} \le 0. \tag{11}$$

Here the post-impact velocity and the mass ratio can be determined through semi-empirical equations. In order to find the most relevant and efficient models to implement SLD wall interaction in the shallow water droplet equation system, an extensive literature review was conducted with a focus on the primary selection criterion, the applicability to real aircraft flight icing problems. A physical model was proposed by Bai and Gosman [23] for the rebound phenomena in droplet impingement, along with a transition regime threshold based on droplet properties and surface properties. This model is applicable for both a dry surface and wet surface and classifies the droplet impingement phenomena into four regimes: stick, rebound, spread and splash, as summarized in Fig. 1 (right). The regimes are specified by the impact Weber number, and the Laplace number. The model defines four distinctive regimes: 1) stick if $We_s \le 2$; 2) rebound if $2 < We_s \le 10$; 3) spread if $10 < We_s \le 1320La^{-0.183}$; and 4) splash if $We_s \ge 1320La^{-0.183}$. In the

model, the velocity ratio (f_u= u_s/u_0) associated with particle rebound off a solid surface is given by

$$f_{u,t} = \frac{u_{t,s}}{u_{t,0}} = \frac{5}{7}, \quad f_{u,\mathrm{n}} = \frac{u_{n,s}}{u_{n,0}} = -\left[0.9930 - 1.76\theta_0 + 1.56\theta_0^2 - 0.49\theta_0^3\right]. \tag{12}$$

The splashing is another regime in the droplet wall interaction which is modeled using Trujillo *et al.* [24] model. The following expression determines the droplet secondary velocity components:

$$f_{u,t} = \frac{u_{t,s}}{u_{t,0}} = \left(0.85 + 0.0025\theta_0\right), \quad f_{u,\mathrm{n}} = \frac{u_{n,s}}{u_{n,0}} = -\left(0.12 + 0.0020\theta_0\right). \tag{13}$$

Finally, the ratio between the ejected mass and initial mass of the droplet accounts for the mass loss at the wall due to droplet splashing is modeled using the Yarin and Weiss [25] expressions,

$$f_m = \frac{m_s}{m_0} = 0.8\left\{1 - \exp\left[-0.85\left(K_y - 17\right)\right]\right\} \tag{14}$$

where

$$K_y = 0.45^{-\frac{3}{8}}\left(Oh^{-\frac{2}{5}}We_S\right)^{\frac{5}{16}}.$$

The calculated mass ratio and post-impact velocity from the wall interaction models are then used in the droplet wall boundary conditions as shown in equation (11).

4. Results and Discussion: Performance Degradation of Multi-element Airfoils under Critical SLD Conditions

The multi-element airfoil used for the current investigations was tested for air flow in the NASA Langley Low Turbulence Pressure Tunnel (LTPT), and for droplet impingement in NASA's Glenn's Icing Research Tunnel (IRT), respectively [26, 27]. The arrangement of the three-element airfoil is illustrated in Fig. 3 and the parameter values are given in Table 1.

The stowed chord c = 32 inch		
Slat chord	C_s	0.15c
Main-element chord	C_{me}	0.83c
Flap-chord	C_f	0.3c
Slat deflection angle	δ_{slat}	30^o

Flap deflection angle	δ_{flap}	30^{o}
Slat gap	Gap_{slat}	2.95%
Flap gap	Gap_{flap}	1.25%
Slat overhang	OH_{slat}	2.5%
Flap overhang	OH_{flap}	0.5%

Table 1. The geometrical parameters of multi-element airfoil

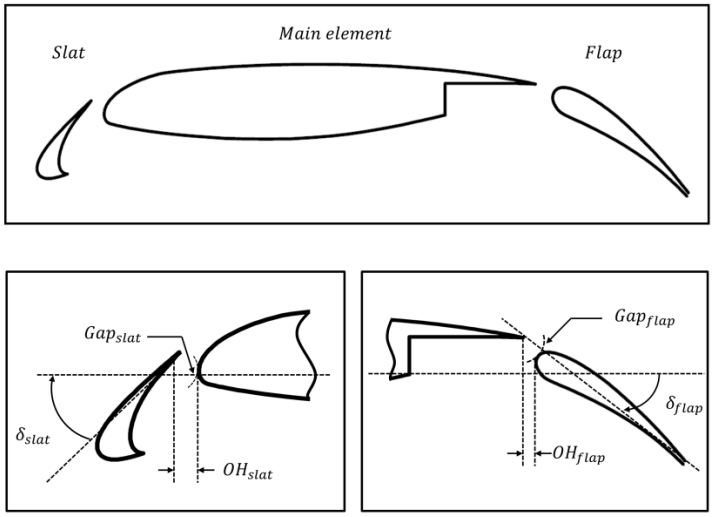

Figure 3. Three-element high-lift airfoil geometric parameters

4.1. Grid independence study

A grid independence study was conducted to establish accurate results and to keep the computation cost low. Three different meshes are used for the grid independence study with a growth rate of 1.01, 1.03, and 1.08. The standard wall function method was used in order to avoid the requirement of a very fine grid close to the wall. Fig.4 (right) shows the pressure coefficients calculated for three different meshes. The difference for mesh-2 and mesh-3 grids turned out negligible, allowing the use of the mesh-2 for further calculations. The maximum Y+ value corresponding to the mesh-2 is 45. The mesh used for the current simulations (mesh-2) is shown in Fig 4 (left).

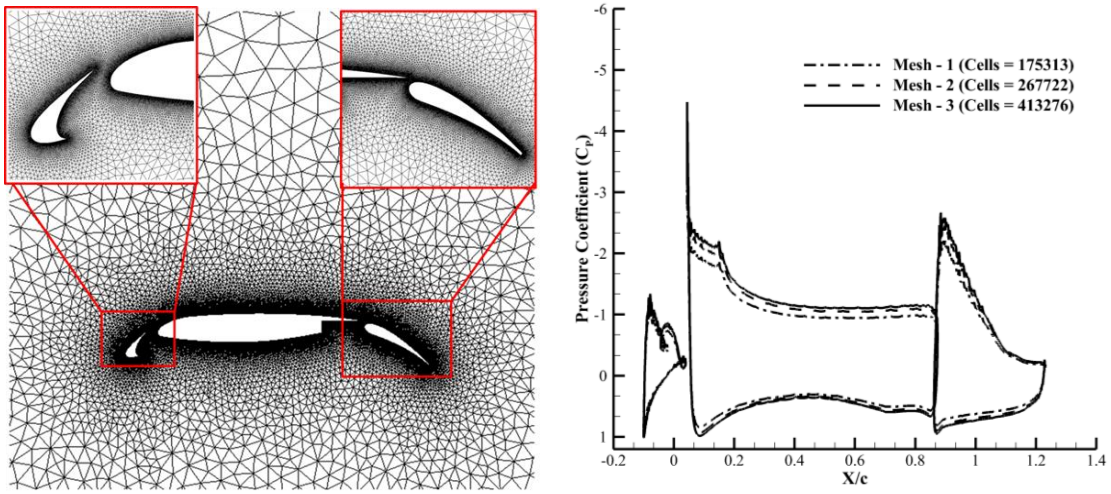

Figure 4. Grid distribution (left) and comparison of pressure coefficient (right) around the multi-element on different meshes

4.2. Validation of current models of aerodynamics, droplet dynamics, SLD-wall interactions, and ice accretion

The unified computational approach based on the second-order positivity-preserving unstructured upwind finite volume method is validated for the multi-element airfoil case. The computational solutions were obtained for a multi-element airfoil at a Mach number of 0.23, and an angle of attack (α) of 4 degrees. The metrological conditions used for the analysis were the static temperature, 276 K, liquid water content (LWC), 0.15 g/m^3, and droplet diameter (MVD), 21 μm.

Further, an SLD case with a droplet diameter of 92 μm (LWC of 0.19 g/m^3) was simulated to show the capability of the unified approach on a multi-element airfoil under SLD icing conditions. The pressure and lift coefficients measured by the experiment were compared with the computational results of the clean air solver. Then, the collection efficiency obtained by the experiment was used to validate the droplet solver. The local collection efficiency is defined as the normalized influx of water at a given location, $\beta = (\rho \mathbf{u} \cdot \mathbf{n} \,/\, \mathrm{LWC} \cdot U_\infty)\, \beta_{Collector}$, where the $\beta_{Collector}$ is a variable depending on MVD [27]. Thus it can quantitatively measure the potential of droplets to collect and the subsequent ice-accretion.

Multi-element airfoils with very small gaps complicate not only the general flow structures but also the generation of the computational mesh. In particular, *the boundary layer transition,*

flow separation, and interaction of wakes can cause severe computational challenges in the simulation of multi-element airfoils. The circulation of the slat induces an accelerated flow around the leading edge of the main element which delays the separation of the main element. On the other hand, the main element induces a circulation effect on the slat element which increases the lift. Further, the flow over the flap element is formed in combination with the wake of the slat and main element, and a boundary layer of the flap itself. In multi-element airfoils, while each element has its own boundary layer, the wake of the forward element can interact with the boundary layer of the corresponding element, leading to a thick merged boundary layer. The important flow features related to strong interactions and liquid water content around the multi-element airfoils are illustrated in Fig. 5.

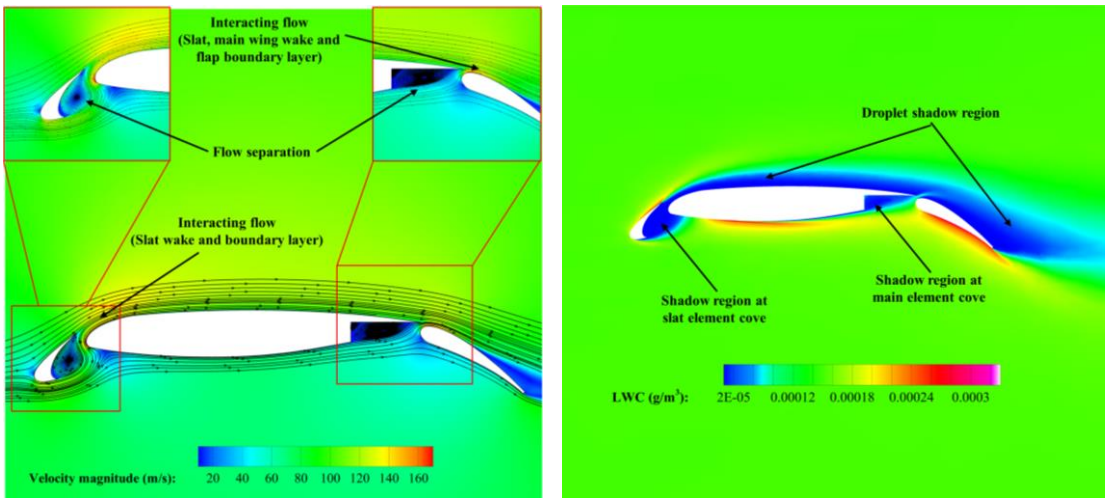

Figure 5 Air velocity magnitude (left) and LWC (right) around the multi-element airfoil at $\alpha = 0$, M = 0.23, T_∞ = 268 K, LWC = 0.15 g/m^3, MVD = 21 μm

Owing to the complexity of the multi-element geometry, methods used by previous studies [28, 29] (panel or potential flow solvers) are not feasible. Hence, a robust computational model is essential to investigate the complicated flow phenomena in multi-element airfoils. Improper modeling of droplet could easily result in a numerical break-down due to the strong circulation and flow separations on the slat and the main element cove. Moreover, careful assessment of source terms is also necessary to avoid any numerical breakdown of the shallow water droplet equations. The liquid water content shown in Fig. 5 (right) demonstrate that the shadow region with a very low density of the LWC forms at the upper side, the cove region of the slat, and the

cove region of the main element. The larger shadow region found on the upper side of the main element is due to the effect of the freestream angle of attack and presence of slat.

Figure 6 shows the pressure coefficient over the multi-element airfoil. In these clean air flows, good agreement was found for pressure coefficients between the computational and experimental results, demonstrating that the present compressible Navier-Stokes-Fourier solver is capable of producing clean air information.

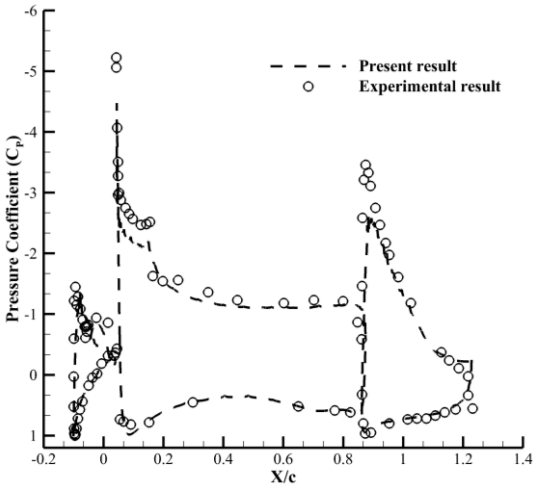

Figure 6 Pressure coefficient around the multi-element airfoil at $\alpha = 0$, M = 0.23, Re = 4.9 million

Figure 7 depicts the collection efficiency around the multi-element airfoil for the non-SLD and SLD meteorological conditions. The collection efficiency increases with the droplet diameter, since the droplet diameter directly affects the impingement area, leading to a higher impingement area in the SLD case. This result has to be taken into account during the design of proper IPS. The impingements of droplets are higher on the leading edge of the slat and the pressure side of the flap, while the main-element does not acquire significant impingements due to the presence of the leading edge slat.

Overall, the computational results are in reasonably good agreement with the experimental data, and in particular, the maximum value of the droplet impingement intensity and the impingement area. Nonetheless, the collection efficiency on the flap is slightly under-predicted in both non-SLD and SLD cases. It is also notable that, in the SLD case, the collection efficiency is over-predicted on the slat surface, while it is under-predicted on the main element. This

discrepancy may be due to the difference in droplet distribution; it was mono-disperse in the computation versus 27 bins of spray cloud drop distributions in the experiment. It is worth mentioning the other probable reasons behind these discrepancies. In the current computations, only the droplet drag and wall interactions models are included. Other complicated SLD effects such as droplet break-up, terminal velocity of the droplet, and the re-impingement of the splashed droplets are not included. Some previous studies on single element [30] mentioned that the accuracy of collection efficiency could be enhanced by implementing re-injection of splashed and rebound droplets, and by increasing the number of droplet bins. Further, the semi-empirical equations used for the droplet deformation and wall interactions might also have some influence on these discrepancies.

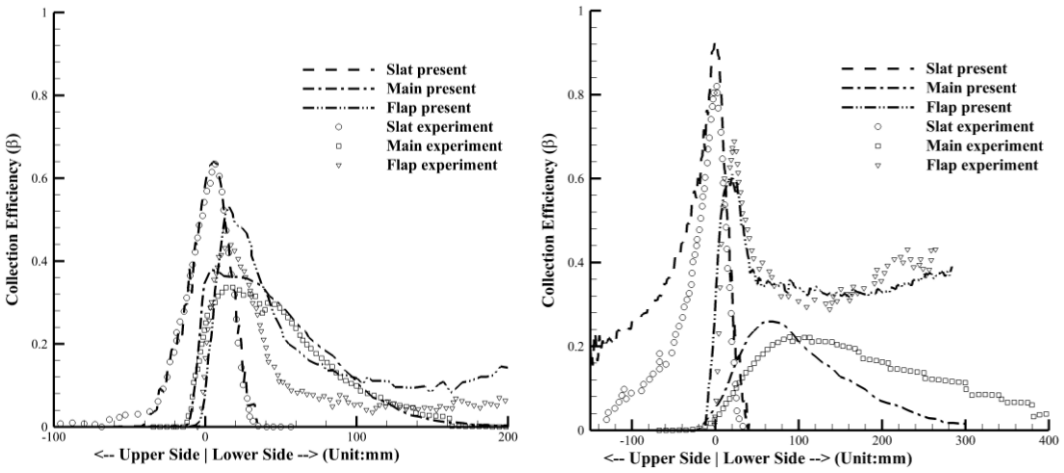

Figure 7 Comparison of collection efficiency around the multi-element airfoil for non-SLD (left) and SLD (right) cases at $\alpha = 4$, M = 0.23, T_∞ = 276 K, LWC = 0.15 g/m^3, MVD = 21 μm (non-SLD case) and LWC = 0.19 g/m^3, MVD = 92 μm (SLD case)

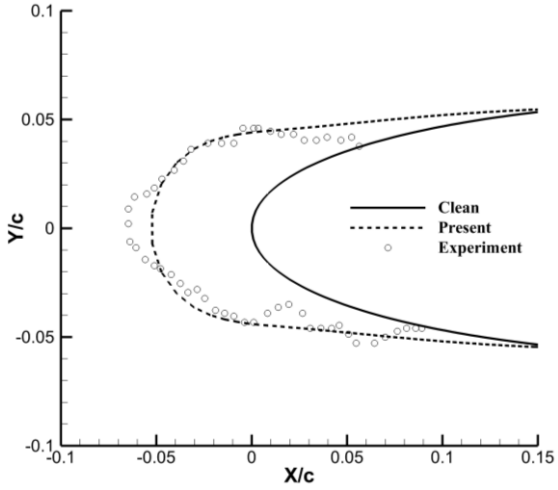

Figure 8 Comparison of ice shape on the NACA 0012 airfoil at $\alpha = 0^o$, M = 0.24, T_∞ = 253.95 K, LWC = 0.65 g/m^3, MVD = 70 μm, and exposure time = 714 sec.

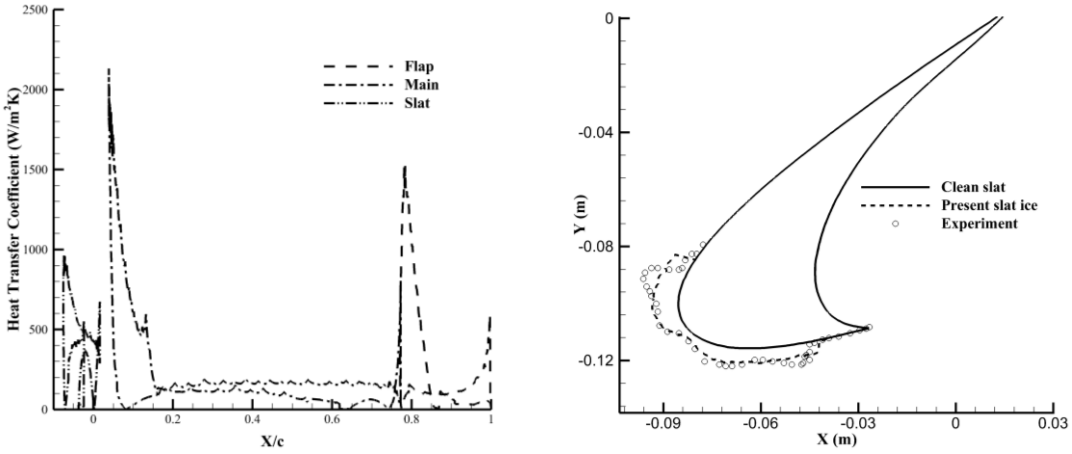

Figure 9 Heat transfer coefficient on the multi-element airfoil (left) and comparison of ice shape on the slat (right) at α = 8, M = 0.26, T_∞ = 268.2 K, LWC = 0.6 g/m^3, MVD = 20 μm

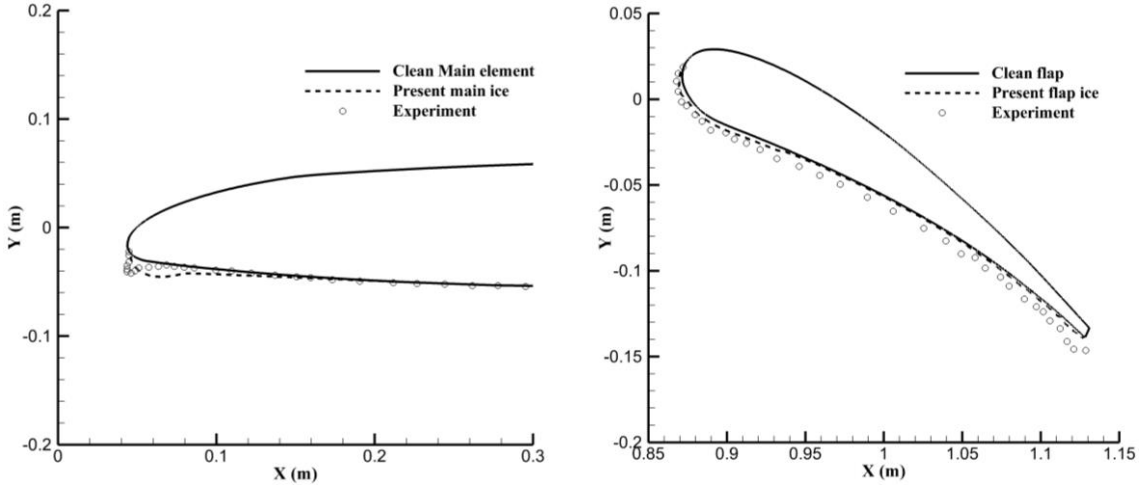

Figure 10 Comparison of ice shape on the main (left) and flap (right) element at α = 8, M = 0.26, T_∞ = 268.2 K, LWC = 0.6 g/m^3, MVD = 20 μm

Further, for ice accretion validation, due to the lack of experimental data on multi-element airfoil configurations under SLD icing conditions, a non-SLD icing condition was used. Nonetheless, the ice accretion under SLD metrological condition is validated using a single element experimental result [31]. Figure 8 illustrates the ice shape comparison of the present and experimental results under SLD icing conditions. The overall simulated ice thickness is qualitatively matching well with the experimental result. However, there are some discrepancies in the leading edge ice thickness, which may be reduced by using multi-shot ice accretion modeling. Figure 9 describes the heat transfer coefficient distribution over the multi-element airfoil and the comparison of ice shapes accreted on the slat. Since the heat transfer coefficient involves convective and evaporative cooling, it can significantly alter the ice shape and the amount of ice accretion on the solid wall surface. Hence, accurate information of heat transfer coefficient is necessary for the ice accretion solver.

The comparison of ice shapes on the slat shows that the present prediction is in close agreement with experimental data. Figure 10 also compares the ice shapes of main and flap element obtained by current ice accretion computational solver and experimental measurement.

In general, for the given metrological conditions, the predicted ice shapes are qualitatively well matched with the experimental data. It is worth noting from Figs. 9 and 10 that the ice thickness on the leading edge of the slat and the flap show good agreement with the experiment. The main factors of ice shape, such as horn thickness and horn angle, are predicted much closer to experimental data.

4.3. Ice accretions and aerodynamic effects on a multi-element airfoil under SLD conditions

Understanding the degradation of the aerodynamic performance of lifting surfaces under icing environments, and designing proper IPS, are challenging tasks in the development of a multi-element wing. Based on the current computational method validated for the various aforementioned cases, an attempt was made to investigate the air flow further, the collection efficiency, ice accretion, and performance degradation on an iced multi-element airfoil under various metrological conditions, ranging from conventional to SLD icing conditions, in

particular. The metrological conditions used for the multi-element airfoil performance study are summarized in Table 2. Figure 11 shows the study validating the performance of clean multi-element airfoils at a Mach number of 0.26, temperature 270.3 K, and Reynolds number 4.9 million. The comparison of lift coefficient on clean airfoil demonstrates an excellent agreement with the experimental data. When the results were compared with the lift coefficient for a clean airfoil, there was excellent agreement with the experimental data.

	LWC (g/m^3)	MVD (μm)	Velocity (m/s)	Angle of attack (degree)	Temperature (K)	Time (mins)
Non-SLD case	0.6	30	88.4	0,4,8,12,16	270.3	15
SLD case 1	0.19	92				
SLD case 2	1.44	154				

Table 2 Metrological conditions used for the multi-element airfoil performance study

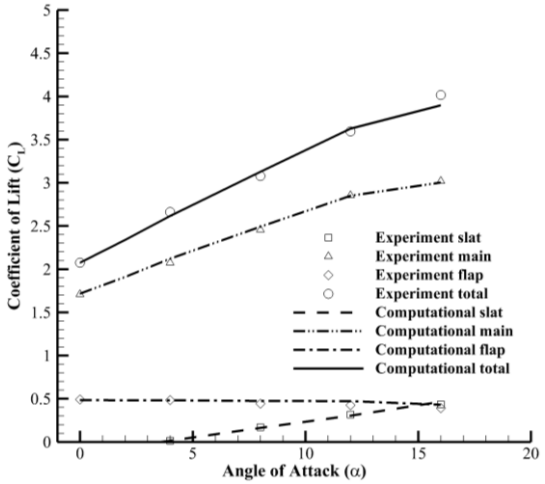

Figure 11 Comparison of lift (left) on a clean multi-element airfoil at M = 0.26, T_∞ = 270.3 K, Re = 4.9 million

Figure 12 shows the ice accretion over the slat and main element in the non-SLD case for various angles of attack. The ice accretion limit of the slat varies drastically with respect to the angle of attack. As expected, more water flows towards the rear part of the stagnation point on the upper surface of the slat at low angles of attack, while the icing limit is significantly reduced on the upper surface of the slat at high angles of attack. The ice accretion on the main element is

negligible at low angles of attack, whereas more runback ice is formed at high angles of attack.

Figure 13 shows the ice accretion over the flap and the subsequent degradation of lift coefficient of the three-element airfoil in the non-SLD case. A maximum lift loss of about 25 percent was found, which is lower than the maximum lift loss of approximately 40 percent known, for single-element airfoils [11]. Ice is uniformly formed only on the lower surface of the flap since the upper surface of the slat becomes a complete shadow region as illustrated in Fig. 3. On the other hand, it was found that the lift coefficient decreases for all angles of attack and all elements. Interestingly, it was observed that *the main element is most responsible for the significant degradation of the lift coefficient* because of its big size, increased roughness, and large ice build-up near the leading edge.

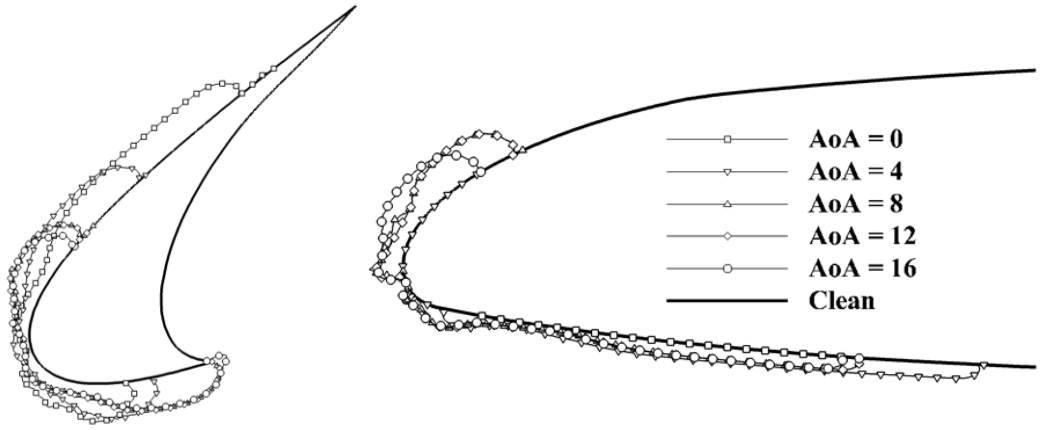

Figure 12 Predicted ice shape on the slat (left) and main element (right) of the three-element airfoil for a non-SLD metrological condition at M = 0.26, T_∞ = 270.3 K, LWC = 0.6 g/m^3, MVD = 30 μm, exposure time = 15 mins

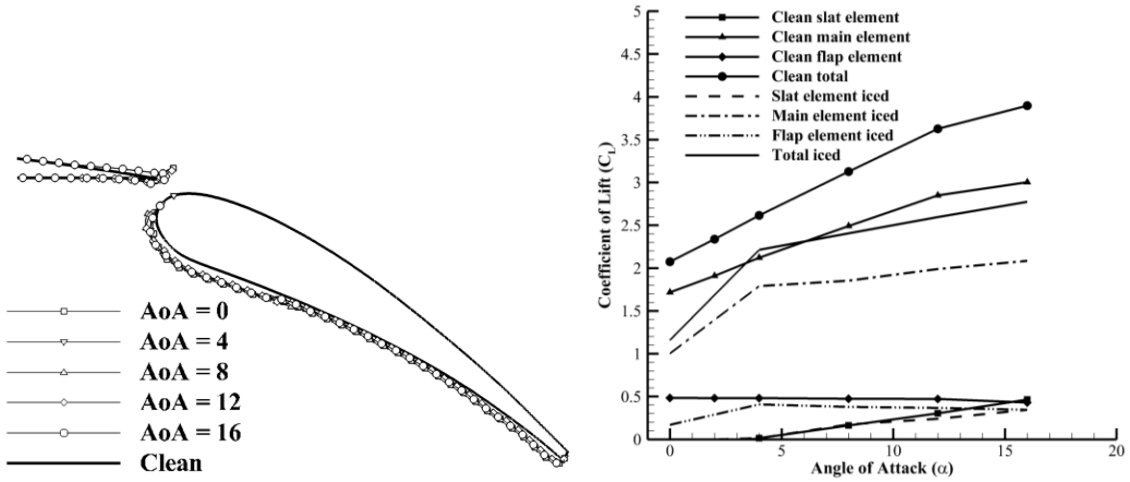

Figure 13 Predicted ice shape on the flap (left) and comparison of the lift coefficient degradation (right) of the three-element airfoil for a non-SLD metrological condition at M = 0.26, T_∞ = 270.3 K, LWC = 0.6 g/m^3, MVD = 30 μm, exposure time = 15 mins

Figure 14 shows the ice accretion on the slat and the main element for moderate SLD case 1. The icing limit on the slat increased considerably when compared with the non-SLD case shown in Fig. 12. It can be noted that the angle of attack has a significant effect on the performance degradation of the multi-element airfoil. The increase in angle of attack shifted the ice accretion towards the lower surface of the slat element. More runback ice also formed on the main element, accreting on more than half of it. Interestingly, the icing limit on the main element changed drastically, and virtually no ice was found at the upper surface of the leading edge, which is a *very surprising counter-intuitive result*. Since there is no horn ice and no formation of irregular shaped ice on the main element, the performance degradation is not expected to be high. This

finding is confirmed from Fig. 15 for the lift coefficient degradation comparison in SLD case 1; a reduction in performance degradation compared with the non-SLD case. In the case of the flap, the icing limit increased with increasing angle of attack. At high angles of attack, more ice was accumulated near the gap between the main element and the flap, indicating the presence of a possible blocking effect due to the ice.

Figures 16-17 show the ice accretion on the slat, the main element, and the flap in severe SLD case 2. They showed a larger, uniformly thick, ice accretion on the slat than the previous two cases, while the ice accretion on the main element did not change much, except for more runback ice on the lower surface of the flap extended to the flap well cove. The combination of higher LWC and very large droplet size may cause significantly higher ice accumulation and broader icing limit on the slat. Furthermore, ice accumulation on the flap was much higher in this severe SLD condition and runback was very high at a high angle of attack. In particular, the gap between the main element and the flap was almost filled with ice accumulated on the flap. The icing limit on the flap increased with increasing angle of attack, leading to most of the upper surface being covered with ice.

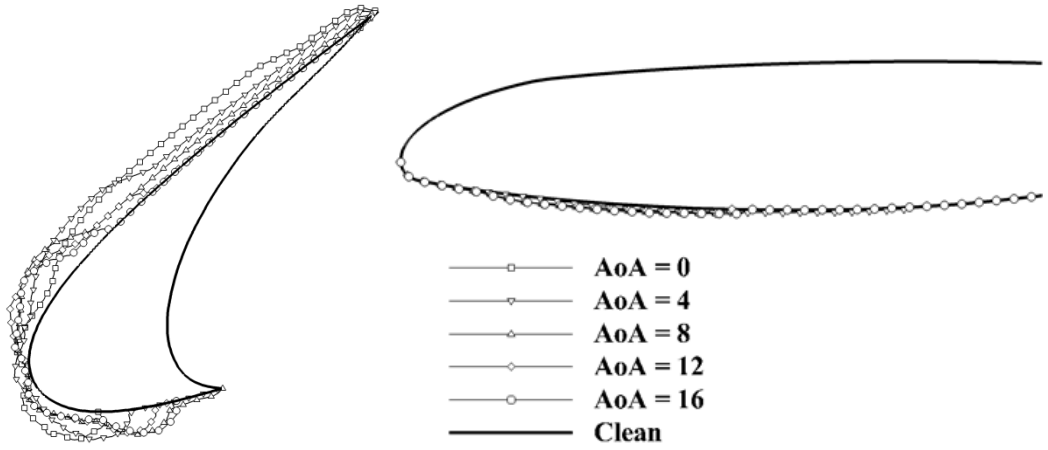

Figure 14 Predicted ice shape on the slat (left) and main element (right) of the three-element airfoil for a SLD metrological condition at M = 0.26, T_∞ = 270.3 K, LWC = 0.19 g/m^3, MVD = 92 μm, exposure time = 15 mins

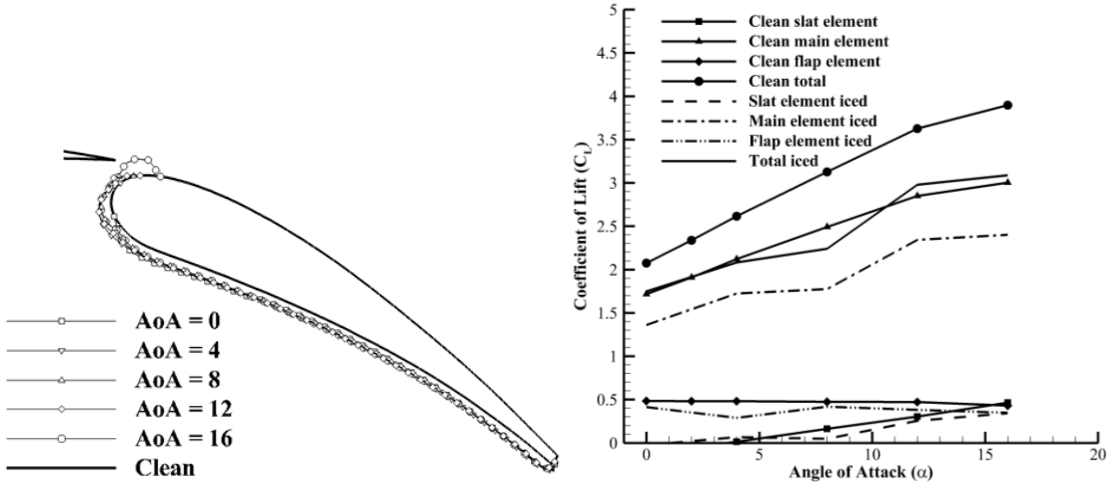

Figure 15 Predicted ice shape on the flap (left) and lift coefficient degradation comparison (right) of the three-element airfoil for a SLD metrological condition at M = 0.26, T_∞ = 270.3 K, LWC = 0.19 g/m^3, MVD = 92 μm, exposure time = 15 mins

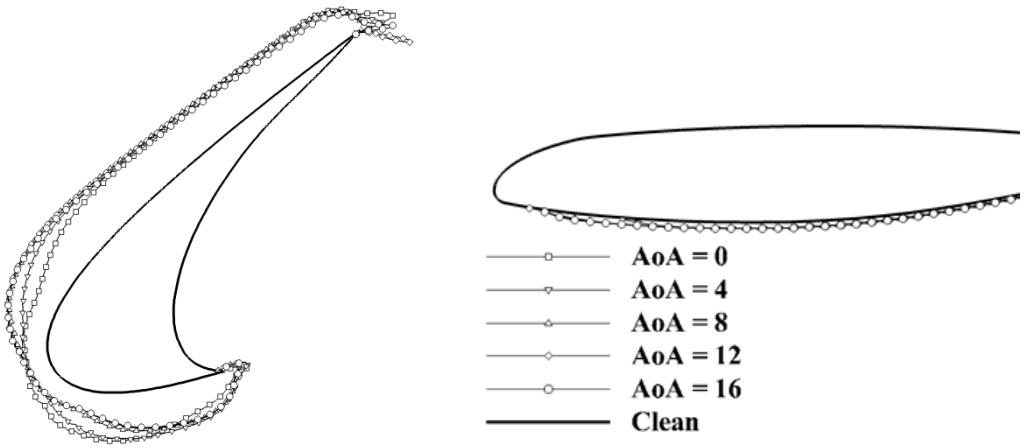

Figure 16 Predicted ice shape on the slat (left) and main element (right) of the three-element airfoil for a SLD metrological condition at M = 0.26, T_∞ = 270.3 K, LWC = 1.44 g/m^3, MVD = 154 μm, exposure time = 15 mins

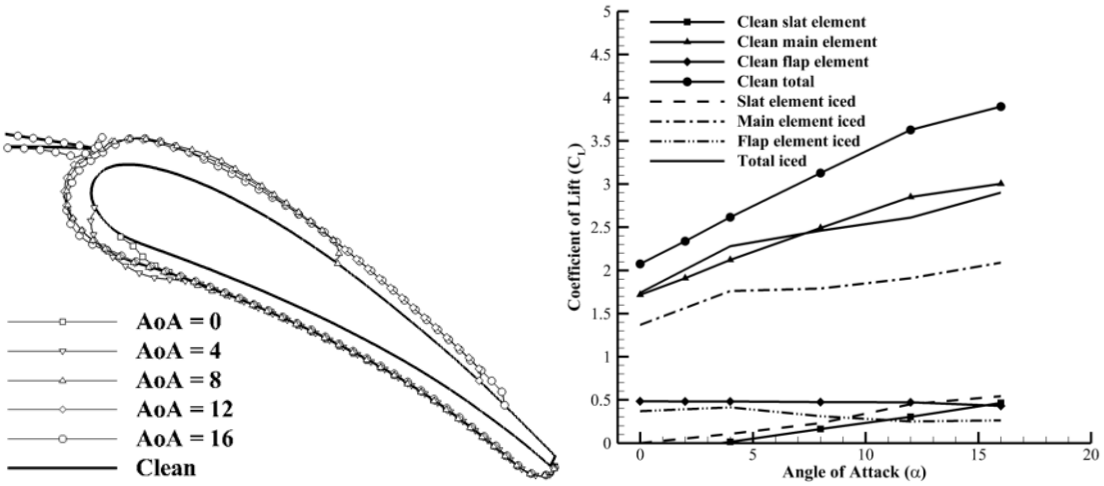

Figure 17 Predicted ice shape on the flap (left) and comparison of lift coefficient degradation (right) of the three-element airfoil for a SLD metrological condition at M = 0.26, T_∞ = 270.3 K, LWC = 1.44 g/m^3, MVD = 154 μm, exposure time = 15 mins

To further investigate the complicated flow physics of multi-element airfoils, the velocity magnitude contours of clean and iced multi-element airfoils are shown in Figs. 18-19 for three different MVD cases (30, 92, 154 μm) and at 16 degrees of angle of attack as an example. In general, the flow shows very complicated patterns consisting of the boundary layer transition, flow separation, and interaction of wakes. In the clean airfoil case, the wake formed on the suction side of the flap is negligible. However, an enlargement in wake and the initiation of flow separation are observed at the suction side of the flap in the MVD 30 μm case. Moreover, due to substantial ice accumulation, the strong flow separation and (primary and secondary) recirculation become apparent in the MVD 154 μm case, and the gap between the main element and flap is severely blocked by ice, which may lead to flight control surface jams.

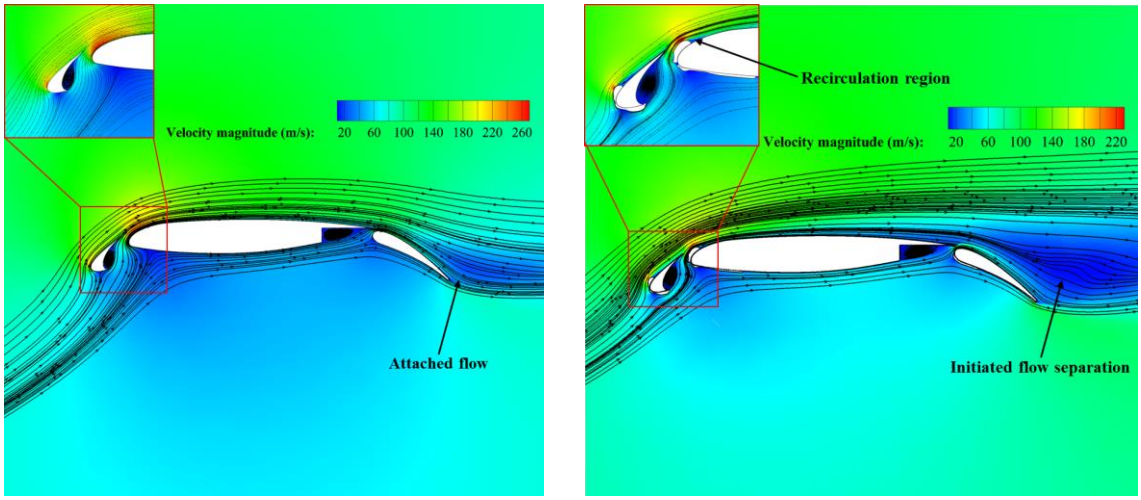

Figure 18 Velocity magnitude and streamlines around clean (left) and iced (right) multi-element airfoils at 30 MVD

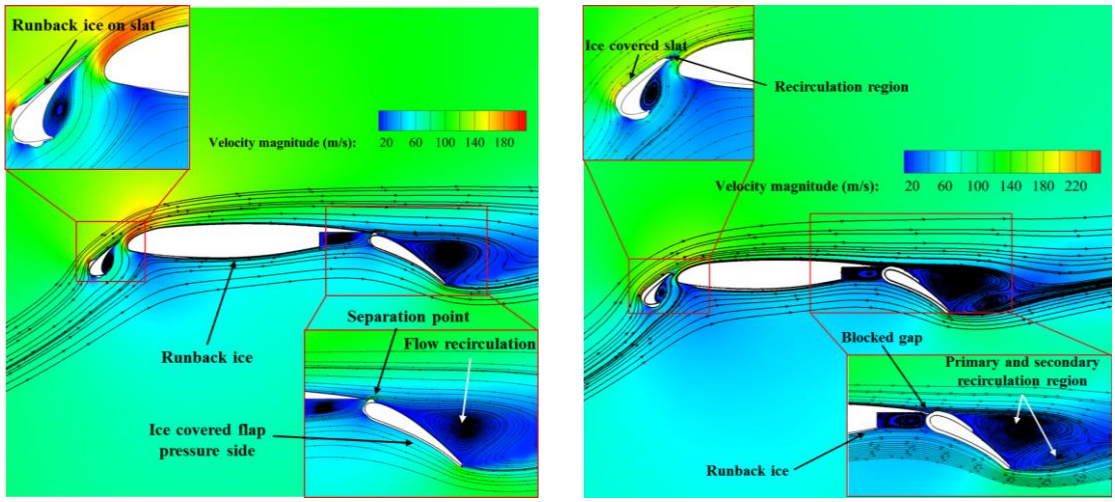

Figure 19 Velocity magnitude and streamlines around iced multi-element airfoils at 92 MVD (left) and 154 MVD (right)

Figure 20 (left) summarizes the total lift coefficients of the multi-element airfoil from Figs. 13, 15, 17. The performance of the multi-element airfoil drops dramatically under all icing conditions. Interestingly, as first noted in Figs. 13 and 15, *the degradation of performance on iced multi-element airfoils is reduced in the SLD cases, in comparison with the non-SLD case, in which immense loss of performance was observed in the main element*. This finding is different from previous studies on iced *single* element airfoils, in which the aerodynamic performance loss was found to be higher for SLD icing conditions than conventional icing conditions [32-34].

Further, the coefficient of drag on clean and iced multi-element airfoils illustrates that the non-SLD icing case generates more drag than the SLD cases. These phenomena may be due to the horn ice at the leading edge of the main element. Moreover, the drag coefficient for SLD

case 2 is much lower than the other two cases. From Figs. 16 and 17 it can be justified that the uniform ice accretion on the slat, main, and flap elements may be the reason behind the reduction of performance degradation under SLD case 2 icing conditions. In summary, in the *multi-element* airfoil case near the freezing non-SLD icing condition, the ice accumulation at the leading edge of the main element alters the entire pressure distribution over the airfoil and the mechanism of lift generation on the main element, leading to a significant loss of performance. In contrast, in the near freezing temperature, more runback ice is formed in the SLD cases, which results in less-deteriorating ice accretion without horns.

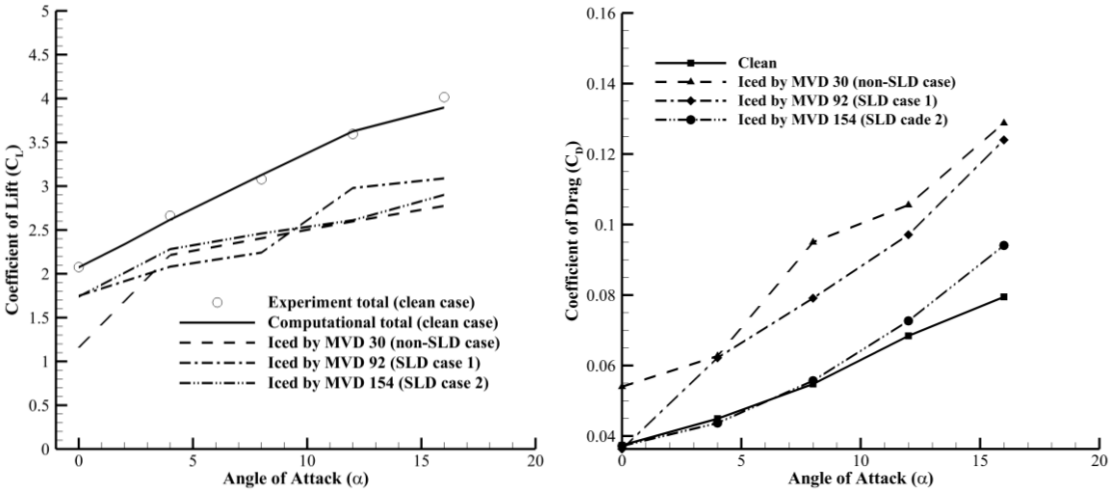

Figure 20 Comparison of lift (Left) and drag (right) coefficient in clean and iced multi-element airfoils for non-SLD and SLD icing conditions at M = 0.26, T_∞ = 270.3 K, exposure time = 15 mins, LWC = 0.6, 0.19, 1.44 g/m^3, and MVD = 30, 92, 154 μm

Since the ice protection system failure time and airplane exit time from the icing clouds prescribed by FAA [35] are 22.5 minutes, a closer exposure time of 15 minutes is selected. Hence, the results provided here can give useful insights into what to expect if the ice protection system failed or was not activated, in particular, in SLD icing conditions. In addition, as the droplet size increases, the droplet impingement limit moves further from the stagnation point to the rear part of the airfoil and it in turn increases the icing limit on the airfoil surface. As a result, droplets do not freeze immediately after impact on the airfoil surface but move backward and freeze gradually.

In summary, the aerodynamic performance of a multi-element airfoil is susceptible to small

variations in the gap size and the overlap between the various elements. Hence, the aircraft designers need to apply necessary precautions to take into account the larger ice accretion on the flap under SLD icing conditions. In addition, the change in icing limit should be considered when designing the ice protection system to ensure there is enough protected area under Appendix O icing conditions.

In particular, careful attention should be paid to the effects of SLD on the slat and flap, since they were found to be more vulnerable to the near freezing SLD icing condition than the conventional icing condition. In the severe SLD case for the slat, more ice accumulated on a wider area of the surface, and thus more energy consumption by the ice protection systems is expected. Also, the possible blocking effect in the gap between the main element and the flap may exist due to uniformly accumulated large ice on the flap.

5. Concluding Remarks

CFD-based aerodynamic, icing, and thermal simulations are being increasingly used for designing the ice protection systems of aircraft, producing artificial ice shapes for certification, and determining the degradation in aerodynamic performance. Further, they are used, in direct and indirect ways, to assist in icing tunnel tests and flight test campaigns.

In this study, these recent developments were employed to investigate a critical issue related to Appendix O, and recently introduced in in-flight icing certification: the SLD effects on the multi (three)-element wing typical of modern transport aircraft.

For this purpose, unified numerical solvers for clean air, large droplet impingement, ice accretion, and aerodynamic analysis of ice effects—all of which are based on a single unstructured second-order positivity-preserving upwind finite volume framework—were first developed and then validated by available experimental data. The study based on the new solvers revealed that the impingement limit in general changed along with the angle of attack, droplet diameter, and ambient temperature. The runback ice was found to be significant in both SLD and non-SLD cases under near freezing temperatures. However, the icing scenarios for slat (coverage of ice) and flap (blocking of the gap with the main element) were found to be more

subtle due to their different positions with respect to the main element.

Interestingly, two counter-intuitive results were found from the comparison of ice accretion and associated aerodynamic degradation in non-SLD and SLD cases. First, in non-SLD conditions, the leading edge (horn-shaped) ice that formed on the suction side of the main element significantly reduced the performance of the main element. In contrast, no leading edge ice formed on the suction side for the SLD condition, leading to a significant reduction in loss of performance. This runs counter to previous studies on iced single element airfoils, in which the aerodynamic performance loss was higher for SLD icing conditions.

Second, it was shown that ice accumulation on the flap was much higher in the SLD conditions and, as a result, the gap between the main element and the flap almost filled with the ice accumulated on the flap, leading to a possible blocking effect.

In summary, it was shown that there is a significant difference in the impingement limit and runback region for the SLD and non-SLD icing conditions on multi-element airfoils. Hence, determining the SLD effects will remain essential in designing the configuration of multi-element airfoils, and a proper ice detection system certified under the Appendices C and O. In future work, the design of thermal-type and electro-thermal-type ice protection systems for multi-element wings and the evaluation of ice growth rate and aerodynamic performance of a swept wing under SLD and non-SLD conditions will be considered.

Acknowledgments

This work was supported by the National Research Foundation of Korea (NRF) Grant funded by the Ministry of Science, ICT & Future Planning (NRF-2017-R1A5A1015311), South Korea.

References

[1] Landsberg B. Safety Advisor: Aircraft Icing. AOPA Air Safety Foundation; 2008.

[2] Jones SM, Reveley MS, Evans JK, Barrientos FA. Subsonic aircraft safety icing study. 2008.

[3] Zhao G, Zhao Q, Chen X. New 3-D ice accretion method of hovering rotor including effects of centrifugal force. Aerospace Science and Technology. 2016;48:122-30.

[4] Lampton A, Valasek J. Prediction of icing effects on the lateral/directional stability and control of light airplanes. Aerospace Science and Technology. 2012;23:305-11.

[5] Ahn GB, Jung KY, Myong RS, Shin HB, Habashi WG. Numerical and experimental investigation of ice accretion on rotorcraft engine air intake. Journal of Aircraft. 2015;52:903-9.

[6] Jung SK, Myong RS. A second-order positivity-preserving finite volume upwind scheme for air-mixed droplet flow in atmospheric icing. Computers & Fluids. 2013;86:459-69.

[7] Petrosino F, Mingione G, Carozza A, Gilardoni T, D'Agostini G. Ice accretion model on multi-element airfoil. Journal of Aircraft. 2011;48:1913-20.

[8] Marwitz J, Politovich M, Bernstein B, Ralph F, Neiman P, Ashenden R. Meteorological conditions associated with the ATR72 aircraft accident near Roselawn, Indiana, on 31 October 1994. Bulletin of the American Meteorological Society. 1997;78:41-52.

[9] Regulations FA. Part 29-Airworthiness Standards: Transport Category Rotorcraft. DOT, FAA, Washington, DC; 1990.

[10] FAA. Engine Certification Requirements in Supercooled Large Drop, Mixed Phase, and Ice Crystal Icing Conditions. Federal Register. 2010;75:37311-39.

[11] Reckzeh D. Aerodynamic design of the high-lift-wing for a Megaliner aircraft. Aerospace Science and Technology. 2003;7:107-19.

[12] Valarezo WO, Lynch FT, McGhee RJ. Aerodynamic performance effects due to small leading-edge ice (roughness) on wings and tails. Journal of aircraft. 1993;30:807-12.

[13] Tan C, Papadakis M. Simulation of SLD impingement on a high-lift airfoil. 44th AIAA Aerospace Sciences Meeting and Exhibit. Reno, Nevada.2006.

[14] Bidwell C. Icing calculations for a 3D, high-lift wing configuration. 43rd AIAA Aerospace Sciences Meeting and Exhibit. Reno, Nevada. 2005.

[15] Zhang C, Wang F, Kong W, Liu H. The Characteristics of SLD icing accretions and aerodynamic effects on high-lift configurations. 33rd AIAA Applied Aerodynamics Conference. Dallas, TX. 2015.

[16] Crow C. Review—Numerical models for dilute gas-particles flows. Trans of ASME Journal of Fluid Engineering. 1982;104:297-303.

[17] Lapple C. Fluid and Particle Mechanics: Vincent Press; 2007.

[18] Messinger BL. Equilibrium temperature of an unheated icing surface as a function of air speed. Journal of the Aeronautical Sciences. 1953;20:29-42.

[19] Cao Y, Ma C, Zhang Q, Sheridan J. Numerical simulation of ice accretions on an aircraft wing. Aerospace Science and Technology. 2012;23:296-304.

[20] Beaugendre H, Morency F, Habashi WG. FENSAP-ICE's three-dimensional in-flight ice accretion module: ICE3D. Journal of Aircraft. 2003;40:239-47.

[21] Morency F, Beaugendre H, Baruzzi G, Habashi W. FENSAP-ICE-A comprehensive 3D simulation system for in-flight icing. 15th AIAA Computational Fluid Dynamics Conference. Montreal, Canada.2001.

[22] Cliff R, Grace J, Weber M. Bubbles, Drops and Particles. Academic Press Inc., New York; 1978.

[23] Bai C, Gosman A. Development of methodology for spray impingement simulation. SAE Technical Paper; 1995.

[24] Trujillo M, Mathews W, Lee C, Peters J. Modelling and experiment of impingement and atomization of a liquid spray on a wall. International Journal of Engine Research. 2000;1:87-105.
[25] Yarin A, Weiss D. Impact of drops on solid surfaces: self-similar capillary waves, and splashing as a new type of kinematic discontinuity. Journal of Fluid Mechanics. 1995;283:141-73.
[26] Valarezo WO, Dominik CJ, Mcghee RJ. Reynolds and Mach number effects on multielement airfoils. NASA Langley Research Center; 1992.
[27] Papadakis M. Experimental investigation of water droplet impingement on airfoils, finite wings, and an S-duct engine inlet. National Aeronautics and Space Administration, Glenn Research Center; 2002.
[28] Hedde T, Guffond D. ONERA three-dimensional icing model. AIAA Journal. 1995;33:1038-45.
[29] Wright WB. Validation Results for LEWICE 3.0. NASA Glenn Research Center; 2005.
[30] Hospers J, Hoeijmakers H. Eulerian method for ice accretion on multiple-element airfoil sections. 48th AIAA Aerospace Sciences Meeting. Oriando, Florida.2010.
[31] Wright W, Potapczuk M. Semi-Empirical Modelling of SLD Physics. 42nd AIAA Aerospace Sciences Meeting and Exhibit. Reno, Nevada. 2004.
[32] Lee S, Bragg MB. Experimental investigation of simulated large-droplet ice shapes on airfoil aerodynamics. Journal of Aircraft. 1999;36:844-50.
[33] Lee S, Bragg MB. Investigation of factors affecting iced-airfoil aerodynamics. Journal of Aircraft. 2003;40:499-508.
[34] Bragg MB, Broeren AP, Blumenthal LA. Iced-airfoil aerodynamics. Progress in Aerospace Sciences. 2005;41:323-62.
[35] Cabler S. Aircraft ice protection: AC 20-73A. FAA, Washington, DC; 2006.